



CHORUS

This is the accepted manuscript made available via CHORUS. The article has been published as:

Nonspinning searches for spinning black hole-neutron star binaries in ground-based detector data: Amplitude and mismatch predictions in the constant precession cone approximation

Duncan A. Brown, Andrew Lundgren, and R. O'Shaughnessy

Phys. Rev. D **86**, 064020 — Published 12 September 2012

DOI: [10.1103/PhysRevD.86.064020](https://doi.org/10.1103/PhysRevD.86.064020)

Nonspinning searches for spinning BH-NS binaries in ground-based detector data: Amplitude and mismatch predictions in the constant precession cone approximation

Duncan A. Brown,¹ Andrew Lundgren,^{1,2,3} and R. O’Shaughnessy^{2,4}

¹*Department of Physics, Syracuse University, Syracuse, NY 13244, USA.*

²*Institute for Gravitation and the Cosmos, The Pennsylvania State University, University Park, PA 16802, USA.*

³*Albert-Einstein-Institut, Callinstr. 38, 30167 Hannover, Germany*

⁴*Center for Gravitation and Cosmology, University of Wisconsin-Milwaukee, Milwaukee, WI 53211, USA*

Current searches for compact binary mergers by ground-based gravitational-wave detectors assume for simplicity the two bodies are not spinning. If the binary contains compact objects with significant spin, then this can reduce the sensitivity of these searches, particularly for black hole–neutron star binaries. In this paper we investigate the effect of neglecting precession on the sensitivity of searches for spinning binaries using non-spinning waveform models. We demonstrate that in the sensitive band of Advanced LIGO, the angle between the binary’s orbital angular momentum and its total angular momentum is approximately constant. Under this *constant precession cone* approximation, we show that the gravitational-wave phasing is modulated in two ways: a secular increase of the gravitational-wave phase due to precession and an oscillation around this secular increase. We show that this secular evolution occurs in precisely three ways, corresponding to physically different apparent evolutions of the binary’s precession about the line of sight. We estimate the best possible fitting factor between *any* non-precessing template model and a single precessing signal, in the limit of a constant precession cone. Our closed form estimate of the fitting-factor depends only the geometry of the in-band precession cone; it does not depend explicitly on binary parameters, detector response, or details of either signal model. The precessing black hole–neutron star waveforms least accurately matched by nonspinning waveforms correspond to viewing geometries where the precession cone sweeps the orbital plane repeatedly across the line of sight, in an unfavorable polarization alignment.

I. INTRODUCTION

Ground based gravitational-wave detector networks (notably LIGO [1–3] and Virgo [4, 5]) have performed several searches for the inspiral and merger of binaries containing black holes (BH) and neutron stars (NS) [6–15]. The coalescence of NS-NS, BH-NS, and BH-BH binaries are the most promising sources of gravitational-waves for these networks [16]. For the lowest-mass compact binaries $M = m_1 + m_2 \lesssim 15M_\odot$, the response of the detector to a binary merger with arbitrary masses and spins is well understood [17–23]. To identify the presence and properties of a signal, the classic approach to data analysis on nonspinning binaries has been matched filtering, linearly projecting the data against each member of a *template bank*: a discrete array of signal models, spaced to cover all possibilities with minimal inter-template and template-signal mismatch [24–28]. For nonspinning binaries, the templates needed lie in the two-dimensional signal manifold itself (i.e., in m_1, m_2 or more naturally in the chirp mass $\mathcal{M}_c = M\eta^{3/5}$ and symmetric mass ratio $\eta = m_1m_2/M^2$) [24, 25, 27]. For spinning binaries with more physical degrees of freedom, the added physical parameters require either (i) exact template banks that are impractically large, with a significant increase in computational burden and false alarm rate; or (ii) the use of an approximate *detection template family*, whose waveforms usually at best imperfectly approximate the target waveforms [18–21, 29] but whose template banks are smaller and better understood. Though the more generic BCV detection template family [20] has been applied in previous searches for spinning systems [10, 30], recent studies suggest that it is no more effective than the nonspinning template bank for low-mass single-spin binaries [26]. Current templated searches for the

gravitational-wave signature of low-mass merging binaries are performed using this simple nonspinning bank [12, 13, 15]. However, these results show that searching for generic spinning binaries with a nonspinning search is sub-optimal and further work is needed to construct an optimal search for spinning binaries in Advanced LIGO and Advanced Virgo. Such a search may involve, e.g. a hierarchical combination of a nonspinning search and a search using spinning templates, or a nonspinning search in some regions of the parameter space, with targeted spinning searches in others. To devise the correct strategy, it is essential to understand where and why advanced-detector searches will lose signal-to-noise ratio when searching for spinning binaries using nonspinning waveforms; this is the goal of this paper.

Recent work on binaries where the spin is aligned with the orbital angular momentum has demonstrated that advanced detectors are more sensitive to the effects of spin on the orbital phase than first generation detectors [31]. However, it has been shown that a slightly more generic search would recover all nonprecessing signals well by capturing the phase evolution of generic nonprecessing sources [31]. Nonetheless, a noticeable fraction of these spinning binary mass, spin, and orientation parameters λ are at best poorly matched with nonspinning and even generic nonprecessing templates, some with match lower than $\simeq 0.6$. These large mismatches occur because nonspinning templates cannot capture the effects of spin.

This paper is concerned with binaries where the spin and angular momentum of the binary are *not* aligned. This induces *precession*, causing the orbital angular momentum direction \hat{L} changes with time. Because the instantaneous beam-pattern of the gravitational-wave emission is oriented along \hat{L} , the changing angle between \hat{L} and the line of sight \hat{n} produces

large amplitude and phase modulations that are absent in non-precessing signals. Poor matches with nonspinning templates are disproportionately concentrated in systems that exhibit precession: systems with significant spin-orbit misalignment and asymmetric mass ratio. Conversely, binaries with tight spin-orbit alignment or simply limited variation in $\hat{L} \cdot \hat{n}$ are well-matched by non-precessing templates that capture the effects of aligned spin¹ on the gravitational-wave phase [32–34]. Understanding the effect of precession is key to developing an optimal search for spinning binaries in second-generation gravitational-wave detectors.

In this paper, we investigate the gravitational-wave signal from precessing black hole–neutron star binaries. Except for a short epoch of transitional precession (typically when $|\vec{L}| \simeq |\vec{S}|$; see [35]), these binaries usually undergo *simple precession*, where the orbital angular momentum precesses around the total angular momentum with an ever-increasing opening angle [35]. By investigating the spin evolution equations of Apostolatos et al. [35], we find that opening angle of the precession cone (i.e., the angle between the total angular momentum \vec{J} and the orbital angular momentum \vec{L}) does not expand significantly while the binary’s signal is in the detector’s sensitive band. We perform analytic studies under the assumption that this opening angle is exactly constant; we call this the constant precession cone approximation. We find the gravitational-wave phasing is modulated in two ways. The first way that precession modifies the signal is via a secular change of the gravitational-wave phase. In addition to the effect of orbital dynamics, the gravitational-wave signal also accumulates a geometrical phase, a fraction of the “precession phase” of \vec{L} about \vec{J} . Previous work has demonstrated that precession induces a secular change in the phase accumulating over each precession cycle, both in post-Newtonian studies [19, 35] and in numerical simulations of GR [36]. Though long recognized, this factor is not included in standard analytic non-precessing template models [32–34].² We furthermore find this secular evolution occurs in three different ways, corresponding to physically different apparent evolutions of the precession about the line of sight. These three ways correspond precisely to whether the cone swept out by \vec{L} encloses zero, one, or two of the “null lines”, which are the directions that produce exactly zero instantaneous response in the detector. The three regions correspond to whether zero, one, or both directions are enclosed by the path swept out by \vec{L} – henceforth, the “precession cone.” Each type of configuration leads to a unique effect on the phasing of the binary. If you are within one of the regions, you accumulate secular phase at the same rate.

The second way that precession modifies the signal is by introducing phase (and amplitude) modulations, on top of secular evolution. These modulations cannot be captured by a non-precessing template. A non-precessing signal model will therefore not match a precessing signal optimally. Moreover, the highest possible mismatch between a precessing signal and non-precessing model can be estimated *geometrically*. In other words, our calculation tells us how easily a non-precessing search can find each particular precessing signal. For simplicity, we perform our analytic studies assuming a source directly overhead a single detector. Our results will be generalized to a full network in a future analysis. Though simplified, our study is nonetheless directly applicable to real searches.³ Moreover, given the complexity of realistic searches, special cases where searches have well-understood performance provide invaluable tools for code validation and search calibration. Past, present, and future searches therefore benefit from the goal of this paper: a simple model for how well nonspinning searches recover most spinning, precessing low-mass binaries.

We will perform a detailed point-by-point numerical comparison of this expression to a large-scale Monte Carlo study of synthetic searches in a subsequent publication. To compare with existing results in the literature, however, we apply our purely analytic results to randomly selected binary parameters. We find our expressions quantitatively agree with previous Monte Carlo studies of nonprecessing searches [20, 37], including recent investigations that include both mass and aligned spin as parameters [31]. For instance, adopting the same spin distribution as [31], we reproduce a similar distribution of fitting factors. Unlike previous purely Monte Carlo studies, however, our analytic approach allows us to quantitatively predict precisely which systems are not well fit with nonprecessing templates. The performance of a nonprecessing search on BH-NS systems with any mass and spin distribution can be easily predicted using our amplitude and mismatch predictions, and the simple predictions for the parameters that cause bad matches point the way toward improved searches.

In Section II we demonstrate that BH-NS binaries seen by gravitational-wave detectors will often evolve on a constant precession cone. In Section III we parameterize the ways in which the binary’s precession cone can be oriented relative to a single detector and its line of sight to the source. We find that there are three distinct regions in this configuration space. In Section IV we review the leading-order gravitational-wave emission from a precessing binary, decomposing it into secular and modulated factors. We show how the gravitational-wave signal from each region has a distinctive secular dependence. Finally, in Section V we average the amplitude over the precession cone, relating the mean power seen along the line of sight to the power expected from an optimally oriented source. Additionally, we argue that non-precessing sig-

¹ Aligned spin means that the spins of the compact objects are aligned with the orbital angular momentum. In this case there is no precession.

² The full effects of precession are of course captured in full time-domain calculations of orbit dynamics and precession. These direct simulations, however, are presently too slow to be used in a search. Additionally, no one has constructed a complete template bank (a discrete set of reference signals) that adequately but minimally covers all possible signal options.

³ For example, the two-detector LIGO network is nearly aligned and approximately sensitive to one polarization at a time. In a subsequent paper we will address explicitly how to rescale our results to the two-detector LIGO network.

nal templates necessarily cannot reproduce oscillations in the precessing signal model. Using a similar average and assuming a generic signal model reproduces the *secular* phase, we find an expression for the mismatch between non-precessing and precessing signals.

II. ORBIT DYNAMICS AND THE CONSTANT PRECESSION CONE LIMIT

We consider a binary of two compact objects with masses m_1 and m_2 , with $m_1 \geq m_2$, and intrinsic spins \vec{S}_1 and \vec{S}_2 . From the coordinate separation \vec{r} and the velocity $\vec{v} = \partial_t \vec{r}$, we can define the coordinate Newtonian angular momentum $\vec{L} = \mu \vec{r} \times \vec{v}$, where $\mu = \frac{m_1 m_2}{m_1 + m_2}$ is the reduced mass.

For generic binaries, the orbit and spins evolve according to complicated position-, spin-, and velocity-dependent expressions [32, 38, 39]. Averaging these post-Newtonian spin evolution equations over a few orbital periods leads to adiabatic expressions for the evolution of spin and orbital frequency [see, e.g., [35] (henceforth ACST), Schnittman [39]]:

$$\partial_t \hat{L} = \vec{\Omega}_L \times \hat{L} \quad (1a)$$

$$\partial_t \vec{S}_1 = \vec{\Omega}_{S_1} \times \vec{S}_1 \quad (1b)$$

$$\partial_t \vec{S}_2 = \vec{\Omega}_{S_2} \times \vec{S}_2 \quad (1c)$$

$$\vec{\Omega}_L = \frac{1}{r^3} \left[\left(2 + \frac{3m_2}{2m_1} \right) \vec{S}_1 + \left(2 + \frac{3m_1}{2m_2} \right) \vec{S}_2 - \frac{3}{2|L|} [(\vec{S}_2 \cdot \hat{L}) \vec{S}_1 + (\vec{S}_1 \cdot \hat{L}) \vec{S}_2] \right] \quad (1d)$$

$$\vec{\Omega}_{S_1} = \frac{1}{r^3} \left[\left(2 + \frac{3m_2}{2m_1} \right) \vec{L} + \frac{\vec{S}_2 - 3\hat{L}(\vec{S}_2 \cdot \hat{L})}{2} \right] \quad (1e)$$

$$\vec{\Omega}_{S_2} = \frac{1}{r^3} \left[\left(2 + \frac{3m_1}{2m_2} \right) \vec{L} + \frac{\vec{S}_1 - 3\hat{L}(\vec{S}_1 \cdot \hat{L})}{2} \right] \quad (1f)$$

In this expression we have omitted the quadrupole-monopole term described in [39], to more clearly correspond with the expressions from ACST on which we rely. We have included the spin-spin terms (containing both \vec{S}_1 and \vec{S}_2) for reference but we will soon assume that only one body is spinning. These evolution equations cause \vec{S}_1 and \vec{S}_2 to precess but leave their magnitude constant. The direction \hat{L} of the orbital angular momentum also precesses and gravitational-wave emission causes the length of \vec{L} to shrink as the binary evolves.

As described in ACST, when either one mass is nonspinning (e.g., $\vec{S}_2 \simeq 0$), the component masses are comparable ($m_1 \simeq m_2$), or the smaller mass has a miniscule mass and necessarily spin ($m_1 \gg m_2$), these expressions reduce to effectively *single spin evolution*, meaning equations of motion are equivalent to the dynamics of \vec{L} and a single (effective) spin. For single spin binaries, spin-orbit evolution can occur in effectively two phases: (i) rare *transitional precession* when $\vec{J} = \vec{L} + \vec{S} \simeq 0$, the relative change in \vec{J} is large, and \vec{J} can

change direction; and (ii) *simple precession*, when are nearly constant \vec{L} and \vec{S} precess roughly steadily around \vec{J} .

Single-spin evolution is particularly appropriate for BH-NS binaries. Neutron stars likely do not spin rapidly ($\vec{S}_2 \approx 0$) – observations suggest spin periods of no less than a few milliseconds [40]. Observations and theoretical considerations constrain plausible NS masses to $1 - 3M_\odot$, ensuring the second object’s minimal spin has little impact on the orbit about an a priori higher-mass companion. Albeit with less accuracy, BH-BH systems also often approximately satisfy the single-spin condition, as binaries that are either comparable mass or dominated by a single spinning body occupy most of the $m_1, m_2, \vec{S}_1, \vec{S}_2$ parameter space; see, e.g., the discussion in [18].

A. Simple precession

For the circular orbits expected in astrophysical scenarios, the spin evolution equations usually imply *simple precession*: the orbital and spin angular momenta precess about the total angular momentum, which is fixed, except for negligible precession of its own about its average direction [ACST]. Assuming $\vec{S}_2 = 0$, the system evolves with $\kappa = \hat{L} \cdot \hat{S}_1$ and $|S_1|$ both constant. At early times, the total angular momentum \vec{J} is dominated by and closely aligned with \vec{L} ; as radiation carries away orbital angular momentum, eventually \vec{J} is dominated by and closely aligned with \vec{S} . As the direction of the total angular momentum is nearly conserved, this process involves substantial change in the spin and orbital angular momentum directions. Following ACST, we will employ the ratio of \vec{S}_1 to the Newtonian angular momentum $\vec{L} = \mu \vec{r} \times \vec{v}$ as a parameter:

$$\gamma(t) \equiv |\vec{S}_1|/|\vec{L}(t)| = \frac{\chi_1 m_1^2}{\eta M \sqrt{Mr(t)}} \quad (2)$$

Using this parameter, the opening angle β of the precession cone (denoted λ_L in ACST) can be expressed trigonometrically as

$$\beta(t) \equiv \arccos \hat{J} \cdot \hat{L} = \arccos \frac{1 + \kappa \gamma}{\sqrt{1 + 2\kappa \gamma + \gamma^2}} \quad (3)$$

Note that for a spin-dominated binary ($\gamma \gg 1$) $\kappa = \cos \beta$; for an angular momentum dominated binary ($\gamma \simeq 0$) $\beta \simeq 0$; and for a spin-orbit aligned binary ($\kappa = 1$) all three of the spin, orbit, and total angular momenta are aligned ($\beta = 0$). At the level of accuracy of interest here,⁴ the opening angle $\beta(f)$ at a given gravitational frequency f can be estimated by the above

⁴ As described at greater length in a subsequent publication, our constant precession cone approximation is designed to be accurate to of order several percent in power and mismatch. Quantitative comparisons of our approximation to numerical simulations will be provided in that publication.

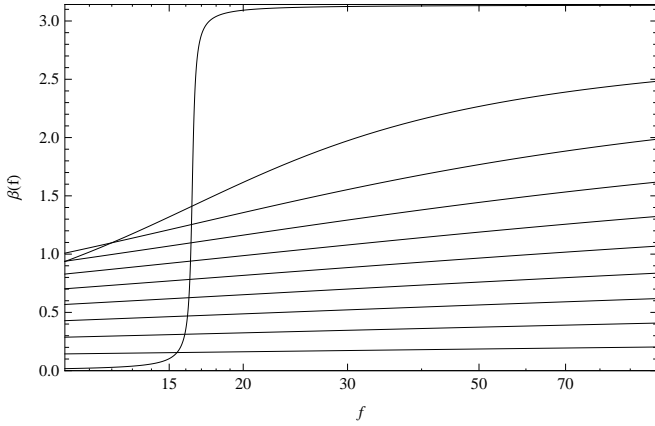


FIG. 1: **Constant precession cone approximation works:** Opening angle $\beta(f)$ versus frequency for a $10M_{\odot} + 1.4M_{\odot}$ binary with $\chi_1 = 1$ and $\arccos \kappa = 0, \pi/10, \dots$ (bottom curves) up to $\arccos \kappa \approx \pi$ (top, rapidly changing curve). We estimate $\beta(f)$ using Eqs. (3,4). This plot shows that except for highly misaligned binaries ($\arccos \kappa$ large), $\beta(f)$ is nearly constant, changing at most a fraction of a radian across the sensitive band of present and future detectors. In general, only a small subset of masses and highly misaligned spins are finely tuned enough to produce significant β evolution in band.

expression, combined with the leading-order Newtonian expression $r(f) = M(M\pi f)^{-2/3}$:

$$\begin{aligned} \gamma &\simeq \chi_1 \frac{(m_1/M)^2}{\eta} (M\pi f)^{1/3} \\ &\approx 2.5\chi_1 (m_1/10m_2) \left(\frac{fM}{100 \text{ Hz } 10M_{\odot}} \right)^{1/3} \end{aligned} \quad (4)$$

Figure 1 shows an example of $\beta(f)$ deduced from this expression.

During simple precession over longer timescales, the width of the precession cone increases on the gravitational-radiation timescale ($\tau_{gw} \simeq [r^4/(\eta M^3)](5/64)$). During this slow increase, the orbital angular momentum traces out an ever-widening spiral at the precession frequency:

$$\partial_t \hat{L} = \left(2 + \frac{3m_2}{2m_1} \right) \frac{\vec{J}}{r^3} \times \hat{L} \quad (5)$$

$$\vec{\Omega}_p = \left(2 + \frac{3m_2}{2m_1} \right) \frac{\vec{J}}{r^3} \quad (6)$$

$$|\Omega_p| = \left(2 + \frac{3m_2}{2m_1} \right) \begin{cases} \frac{\mu}{M^2} (M\pi f)^{5/3} & |\vec{L}| \gg |\vec{S}| \\ \chi_1 \frac{m_1^2}{M^3} (M\pi f)^2 & |\vec{L}| \ll |\vec{S}| \end{cases} \quad (7)$$

where we have replaced r by the leading-order PN expression $v^2 = (M/r) = (M\pi f)^{-2/3}$ and $L_N = \mu M (M\pi f)^{-1/3}$. ACST provide an explicit, algebraic solution for the spins as a function of time [their Eqs. (59-63)].

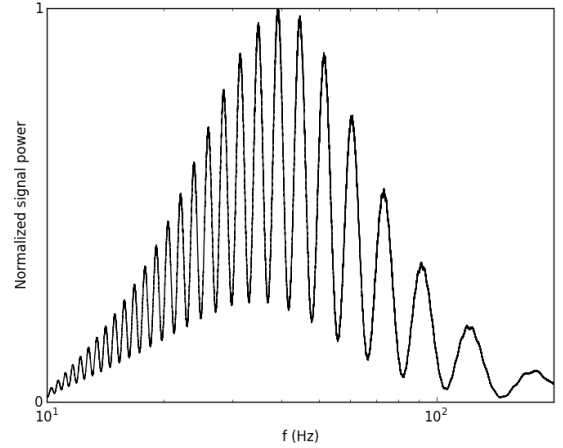


FIG. 2: **Several precession cycles contribute comparably to the signal:** Power ($|\hat{h}_{\times}|^2/S_h(f)$) versus frequency for a spinning binary viewed edge on in the \times polarization, computed directly from a Fourier transform of the gravitational-wave signal. In this figure, the binary is a $10 + 1.4M_{\odot}$ BH-NS binary with $\chi_1 = 1$ and $\beta^* \approx \pi/3$ (solid). Each pair of peaks corresponds to a single precession cycle. The signal is divided by the high-power zero-detune advanced LIGO noise PSD (power spectral density) [41].

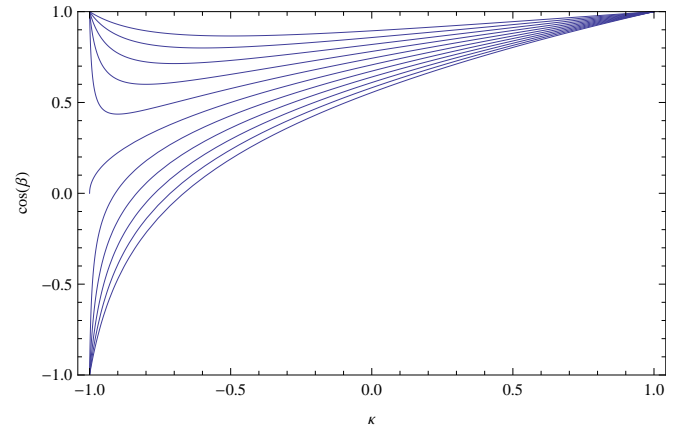


FIG. 3: **Precession opening angle versus spin-orbit misalignment:** Relation between $\kappa = L \cdot S$, and $\beta = \cos^{-1} L \cdot J$ for $\gamma = |S|/|L| = 0.5, 0.6 \dots 1.5$. Binaries that are angular-momentum-dominated ($\gamma < 1$) can have only a small range of precession cone opening angles, bounded by $\beta_{max} = \cos^{-1} \sqrt{1 - \gamma^2}$. Binaries that are spin-dominated ($\gamma > 1$) can have all possible precession cone opening angles. For extremely spin-dominated binaries $\kappa = \cos \beta$.

B. Regions of parameter space I: L,S, dominated or intermediate

Single-spin binaries can be loosely subdivided into rare transitional precession and ubiquitous simple precession [ACST]. In band, simple precessing binaries can be either \vec{L} or \vec{S} dominated. A spin-dominated binary can have an arbitrary opening angle. An \vec{L} dominated binary, by contrast, has a precession cone opening angle necessarily smaller than $\pi/2$,

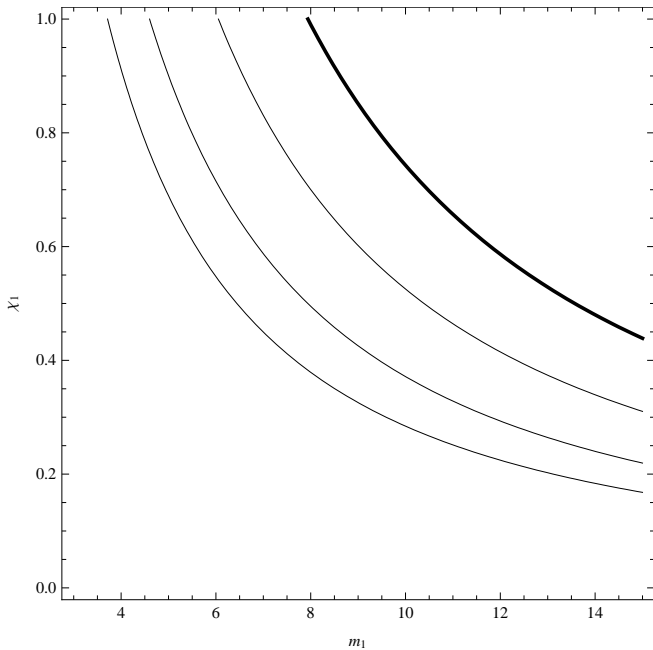


FIG. 4: Angular momentum dominated versus spin-dominated binaries: In terms of the mass and spin of the black hole, contours of the ratio $\gamma = |\vec{S}|/|\vec{L}|$ evaluated at 40 Hz. The bottom left region is angular-momentum dominated ($|\vec{L}| \gg |\vec{S}|$); the top right region of large black hole mass and spin is strongly spin-dominated ($|\vec{S}| \gg |\vec{L}|$). Contours show the ratio $|\vec{S}|/|\vec{L}| \equiv \gamma = 1$ (thick curve), $\sin \pi/4 = 1/\sqrt{2}$, $\sin \pi/6 = 1/2$ and $\sin \pi/8$, evaluated with a $1.4M_{\odot}$ NS companion, versus the black hole mass and spin parameters m_{BH}, χ_{BH} . Above (below) the thick curve, BH-NS binaries' total angular momenta are spin (orbit) dominated in band. If spin and orbital angular momenta are nearly antialigned, these binaries have undergone precession at lower frequencies, typically not in band. Conversely, for orbital-angular-momentum-dominated binaries ($\gamma < 1$), transitional precession has not occurred in the past at lower frequencies and may, if anti-aligned and γ near 1, occur in band in the immediate future. Finally, below the bottom curve, BH-NS binaries waveforms are modulated little by precession in band.

and bounded above by

$$\beta_{max} \equiv \sin^{-1} \gamma. \quad (8)$$

In the neighborhood of this extreme misalignment, at $\kappa = -\gamma$, the opening angle is nearly stationary with spin-orbit misalignment (i.e., $d \cos \beta / d\kappa \simeq 0$). In short, a distribution of \vec{L} dominated binaries has two choices for spin-orbit misalignment (i.e., two values of κ) consistent with each realized opening angle. Additionally, because of the local maximum in β as a function of κ , a randomly oriented distribution of spins will have opening angles β that cluster near that maximum (i.e., $\beta \simeq \beta_{max}$). To illustrate which regions are \vec{L} and \vec{S} dominated, Figure 4 shows contours of constant γ , assuming $m_2 = 1.4M_{\odot}$.

C. Regions of parameter space II: Steady precession and geometry

Unless transitional precession happens in band, ground-based gravitational-wave detectors are sensitive to emission from a relatively well-defined epoch: the precession cone has relatively constant opening angle [Fig. 1]. Quantitatively, we define a reference frequency f_{peak} corresponding to the frequency up to which half of the signal power has been accumulated. The specific reference frequency depends on the noise curve adopted.⁵ For this paper, we adopt the fiducial advanced LIGO noise curve with zero-detuned signal recycling; see [41]). This includes a low-power mode for which $f_{peak} \simeq 40$ Hz and high-power for which $f_{peak} \simeq 60$ Hz. However, all planned noise curves we have examined have a reference frequency in the neighborhood of which a constant precession cone is a good approximation. Henceforth the ratio $\gamma = |S_1|/|L|$ and opening angle β between \hat{L} and \hat{J} will refer to quantities predicted at this frequency by the simple precession expressions [Eqs. 4,3].⁶

Second, not only is the precession cone nearly fixed, but as shown in Figure 2 at least a few complete precession cycles occur between 20 – 100 Hz, where most of the signal-to-noise accumulates. For example, for an angular-momentum-dominated binary ($\gamma \ll 1$), the number of precession cycles for a single-spin binary can be approximated by the spin-independent expression

$$\begin{aligned} N_P &\simeq \int_{\pi f_{min}}^{\pi f_{max}} df_{orb} \frac{dt}{df_{orb}} \Omega_p \\ &= \frac{5}{96} (2 + 1.5 \frac{m_2}{m_1}) [(M\pi f_{min})^{-1} - (M\pi f_{max})^{-1}] \\ &\simeq \frac{27(1 + 0.75m_2/m_1)}{M/10M_{\odot}} \end{aligned} \quad (9)$$

with a comparable but spin-dependent number for an S-dominated binary ($\gamma \gg 1$); see ACST Eqs. (45, 63) for a general solution. As indicated by Figure 2, each precession cycle usually accumulates a comparable proportion of detectable power (i.e., each pair of peaks is a similar order of magnitude in area). More critically, the figure indicates that at least one and often several precession cycles contribute to the total signal to noise. With many precession cycles, a gravitational-wave detector should be relatively insensitive to the initial value of the precession phase.

For our purposes, then, the binary undergoes *nearly steady simple precession* in band. The instantaneous beam pattern of

⁵ In the text we choose the reference frequency as the half-power point, where $\int f^{-7/3}/S_h(f)df$ reaches half of its total value. Alternatively, the reference frequency can be set by maximizing $d\rho/d \ln f = 4f|\dot{h}(f)|^2/S_h$, or even phenomenologically, in whatever manner is needed for numerically-calculated amplitude and match to reproduce our expressions. For the noise curves considered in this paper, all approaches nearly agree.

⁶ For simplicity, we adopt the leading-order (Newtonian) expression for $r(f)$. Higher order corrections are small.

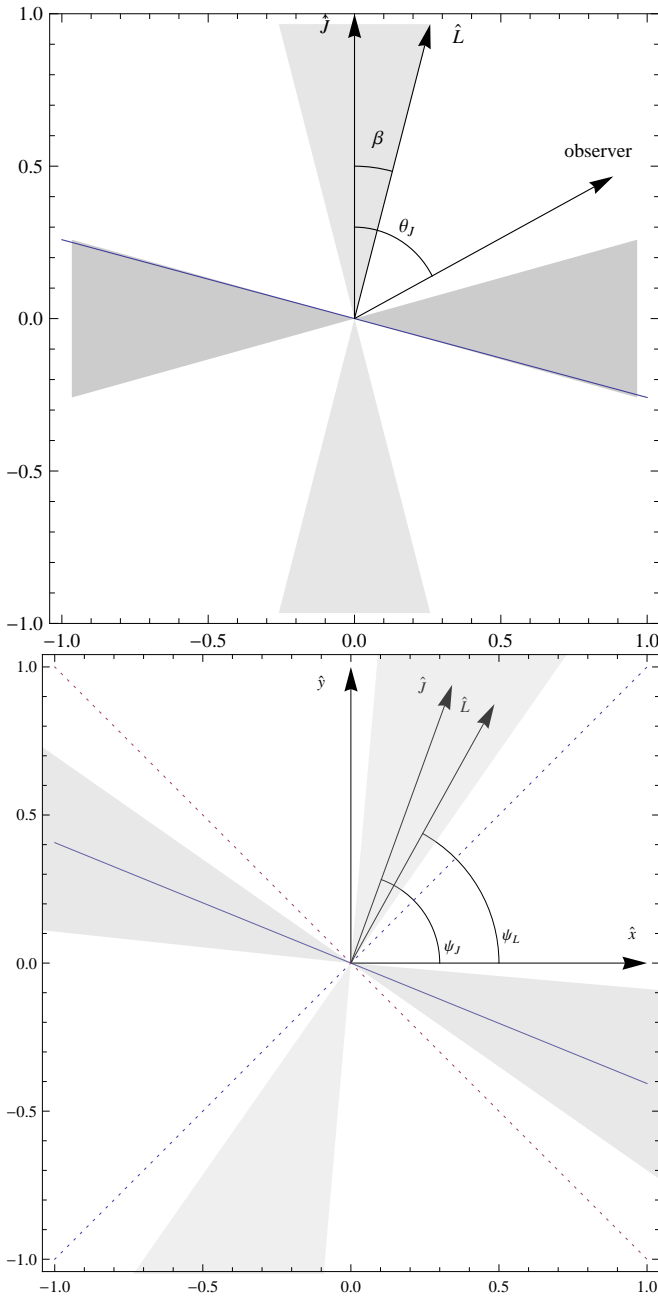


FIG. 5: **Coordinates for steady precession:** View from the side (top panel) and along the line of sight (bottom panel) of the geometry of a typical precessing BH-NS orbit, on timescales t long compared with precession but short compared to gravitational-wave decay ($\Omega_p t \gg 1 \gg t/\tau_{gw}$). The light shaded region indicates the cone swept out around the axis by the orbital angular momentum (the direction of strong, circularly-polarized gravitational-wave emission from each orbit). In both panels, the blue line indicates a direction perpendicular to \hat{L} . The dark shaded region indicates the corresponding region swept out by the orbital plane (the direction of weakest, linearly-polarized emission); observers along these lines of sight see strong amplitude modulation. The angle β between the total angular momentum \vec{J} and \vec{L} is nearly constant on precession timescales. On longer timescales, as β increases, the line of sight to the observer is often enclosed in one of the two shaded regions. On the bottom panel, the \hat{x} and \hat{y} axes correspond to the arms of the detector, projected into the plane of the sky. The dotted lines correspond to “null lines”, the directions that, when \hat{L} is parallel to them, produce zero amplitude in our detector; these lines lie in the plane of the sky, perpendicular to our line of sight. [To distinguish \vec{J} and \vec{L} in the plane of the sky, the two panels adopt different reference times.]

the binary is aligned with the instantaneous \hat{L} , and is the same beam pattern as a non-spinning binary [42]. Along the axis aligned with $\pm\hat{L}$, the radiation is circularly polarized and in the orbital plane, the radiation is linearly polarized. Over a longer timescale, \hat{L} precesses around \hat{J} , sweeping the beam-pattern around the precession cone. Any given line of sight therefore can be characterized with its proximity to the orbital plane (an amplitude minimum and specific, linear polarization) and $\pm\hat{L}$ (an amplitude maximum and specific circular polarizations).

D. Constant precession cone coordinates

In steady precession the unit vector \hat{L} rotates regularly about \hat{J} . In practice, however, we interpret the gravitational-wave strain relative to a frame associated with our line of sight $-\hat{n}$, where \hat{n} is the emission direction from the binary. To simplify calculations, we adopt a frame defined by this direction: $\hat{z} = \hat{n}$, along with two perpendicular directions \hat{x}, \hat{y} . Adopting an initial phase so the projection of L into the plane of the sky (i.e., perpendicular to \hat{n}) is along \hat{J} , the unit vectors needed to describe the steady precession approximation are

$$\hat{J} = \sin \theta_J [\cos \psi_J \hat{x} + \sin \psi_J \hat{y}] + \cos \theta_J \hat{n} \quad (10a)$$

$$\begin{aligned} \hat{p} &= \frac{\hat{J} \times (\hat{J} \times \hat{n})}{|\hat{J} \times (\hat{J} \times \hat{n})|} \\ &= \cos \theta_J [\cos \psi_J \hat{x} + \sin \psi_J \hat{y}] - \sin \theta_J \hat{n} \end{aligned} \quad (10b)$$

Here ψ_J is the orientation of \hat{J} projected into the plane of the sky and θ_J is the angle between \hat{J} and \hat{n} ; see Figure 5. In terms of these vectors, the precession of the orbital angular momentum about \hat{J} can be described as

$$\hat{L} = \cos \beta \hat{J} + \sin \beta R_{\hat{J}}(\alpha) \hat{p} \quad (10c)$$

where $R_{\hat{J}}(\alpha)$ is a rotation operator about \hat{J} and $\alpha = \int \Omega_p dt$ is the precession phase of \vec{L} around that axis [35].

The gravitational-wave strain recovered by a detector depends on the orientation of \hat{L} relative to the radiation frame. In terms of the coordinates above, the inner products needed are

$$\hat{L} \cdot \hat{n} = \cos \beta \cos \theta_J - \sin \beta \sin \theta_J \cos \alpha \quad (10d)$$

$$\begin{aligned} \hat{L} \cdot \hat{x} + i \hat{L} \cdot \hat{y} &= e^{i\psi_J} [\sin \beta (\cos \alpha \cos \theta_J + i \sin \alpha) \\ &\quad + \cos \beta \sin \theta_J] \end{aligned} \quad (10e)$$

$$= e^{i\psi_L} \sqrt{1 - (\hat{L} \cdot \hat{n})^2} \quad (10f)$$

where ψ_L is shorthand for the instantaneous orientation of \hat{L} on the plane of the sky.

For convenience and without loss of generality, in what follows we will assume the binary is directly overhead a single interferometer, with arms along \hat{x} and \hat{y} . For this orientation, the detector response functions are $F_+ = \cos 2\psi_J, F_\times =$

$\sin 2\psi_J$. If the source is not directly overhead, the single-detector response functions

$$F_+ = \frac{1}{2}(1 + \cos^2 \theta) \cos 2\phi \cos 2\psi - \cos \theta \sin 2\phi \sin 2\psi \quad (11a)$$

$$F_\times = \cos \theta \sin 2\phi \cos 2\psi + \frac{1}{2}(1 + \cos^2 \theta) \cos 2\phi \sin 2\psi \quad (11b)$$

can be rewritten as an overall scaling and a polarization shift

$$F_+ = F_0 \cos 2(\psi + \psi_0) \quad (11c)$$

$$F_\times = F_0 \sin 2(\psi + \psi_0) \quad (11d)$$

with

$$F_0 = \sqrt{((1 + \cos^2 \theta)/2)^2 \cos^2 2\phi + \cos^2 \theta \sin^2 2\phi} \quad (11e)$$

$$\tan 2\psi_0 = \frac{\cos \theta}{(1 + \cos^2 \theta)/2} \tan 2\phi. \quad (11f)$$

III. CRITICAL VIEWING ORIENTATIONS AND DOMAINS

The instantaneous emission pattern of gravitational radiation is aligned with the instantaneous orbital angular momentum L and is the same as the beam pattern of a non-spinning binary i.e. an $l = |m| = 2$ quadrupolar configuration. The radiation is circularly polarized along L and $-L$, and linearly polarized in the plane perpendicular to L . In particular, when the orbital angular momentum is instantaneously perpendicular to the line of sight, one (linear) polarization of the gravitational-wave signal is instantaneously zero. The condition that one polarization be zero at some instant defines a two-dimensional surface in the three-dimensional space $(\theta_J, \psi_J, \beta)$ of all possible precession cone geometries. As we show below, this surface decomposes the three-dimensional space into three distinct regions, corresponding to different ways the orbital plane crosses the line of sight or, equivalently, different ways the orbital angular momentum wraps around two null lines.

The detector is not sensitive to (leading-order) gravitational radiation emitted from the binary when the orbital angular momentum simultaneously satisfies the following two conditions:

$$0 = \hat{L} \cdot \hat{n} = 0 \quad (12a)$$

$$0 = (\hat{L} \cdot \hat{x})^2 - (\hat{L} \cdot \hat{y})^2 \quad (12b)$$

Solutions to these expressions exist if and only if the angle between \vec{J} and one of the four critical directions indicated in Figure 6 is equal to the angle β between \vec{J} and \vec{L} , or equivalently if the following expression is zero:

$$d_{null} \equiv (\hat{J} \cdot v_1 - \cos \beta)(\hat{J} \cdot v_1 + \cos \beta) \times (\hat{J} \cdot v_2 - \cos \beta)(\hat{J} \cdot v_2 + \cos \beta) \quad (13)$$

$$= [(\hat{J} \cdot v_1)^2 - \cos^2 \beta][(\hat{J} \cdot v_2)^2 - \cos^2 \beta] \quad (14)$$

where $v_1 = (\hat{x} + \hat{y})/\sqrt{2}$ and $v_2 = (\hat{x} - \hat{y})/\sqrt{2}$. Substituting in the coordinate form for \hat{J} given above and solving $d_{null} = 0$ for $\cos^2 2\psi$ leads to an expression for the boundary polarization angle $\psi_{J,crit}$ between different regions:

$$\begin{aligned} \cos^2(2\psi_{J,crit}) &= \frac{4 \cos^2 \beta (\cos^2 \beta - 1)}{\sin^4 \theta} \\ &= -\frac{(1 + \cos 2\beta)(\cos 2\beta + \cos 2\theta)}{\sin^4 \theta} \end{aligned} \quad (15)$$

These configurations defined above divide the space of orientations $(\theta_J, \beta, \psi_J)$ into five regions, henceforth denoted $R1_\pm$, $R2_\pm$, and $R3$ [Figure 7]. As our notation suggests, using symmetry we can relate two pairs of regions by reflection symmetry $\beta \rightarrow \beta - \pi$. The region $R1$ (the union of $R1_+$ and $R1_-$) corresponds to all configurations such that the orbital angular momentum does not wind around either null line. It includes all points where the orbital plane does not cross the line of sight, plus those connected orientations which never have a null in the waveform amplitude. Due to a coordinate degeneracy in Figure 7, the region shown corresponding to $R1$ consists of two disjoint mirror-image copies $R1_\pm$, related by $\beta \rightarrow \pi - \beta$. These two regions include the special cases of spins aligned or antialigned with the total angular momentum, viewed along or opposite to the total angular momentum. Conversely, the region $R3$ corresponds to binaries and viewing geometries so L winds around *both* null lines. The region $R3$ includes the special case of a *precession disk* ($\beta = \pi/2$), viewed favorably edge on ($\theta_J = \pi/2, \psi_J = 0$), plus those connected orientations free from amplitude zeros. The two regions $R2_\pm$ correspond to the ways L can wind around one or the other null line. At every polarization except $\psi_J = 0$, the regions $R1$ and $R3$ are separated by $R2$. For $\psi_J = 0$, the three regions overlap at the zeros of

$$\cos 2\theta_J + 2 \cos 2\beta + 1 = 2[\sin^2 \theta + \cos 2\beta]. \quad (16)$$

IV. WAVEFORMS IN CONSTANT PRECESSION CONE LIMIT

In this section we review how precession modulates the amplitude and phase of the binary's gravitational-wave signal. We express precession-induced amplitude and phase modulations in terms of a complex factor z . We show the gravitational-wave phase has both oscillating and secularly increasing contributions from precession. The secular effect arises as a fraction of the precession phase is imprinted on the signal. We demonstrate that each of the previously identified regions corresponds to a different amount of secular precession contribution. To leading order, gravitational-wave detection with non-precessing templates works by matching a signal with similar *phase* evolution. In this sense, gravitational-wave signals from each of the three regions are phenomenologically similar (and can be phenomenologically distinguished from one another), as each region has a characteristic secular phase evolution change from precession.

Explicit expressions for the leading-order gravitational waveforms produced by instantaneously stationary orbits are

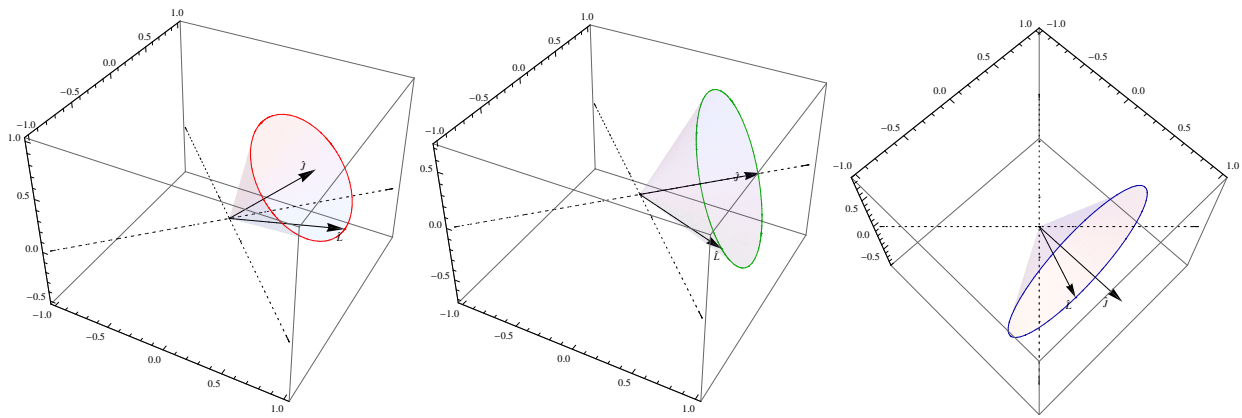


FIG. 6: **Three regions have three types of precession cones:** The figure above shows the precession cone for three fiducial binaries, characterized by the angles $(\theta_J, \beta, \psi_J) = (\pi/4, \pi/6, 0)$, $(\pi/2, \pi/4, \pi/4)$ and $(\pi/2, \pi/3, 0)$. Each figure shows the precession-induced path of $\hat{L}(t)$ (colored circles), the total angular momentum direction (arrow), and an example of an instantaneous L direction (arrow). As these three examples demonstrate, each region corresponds to a different way the precession cone wraps around the two dotted lines. These two lines correspond to orientations of \hat{L} such that the detector would instantaneously see exactly zero amplitude. We will henceforth denote them as “null lines”. These three precession cones are representative examples of the three regions discussed in the text: R1 (left panel), R2 (center panel) and R3 (right panel)

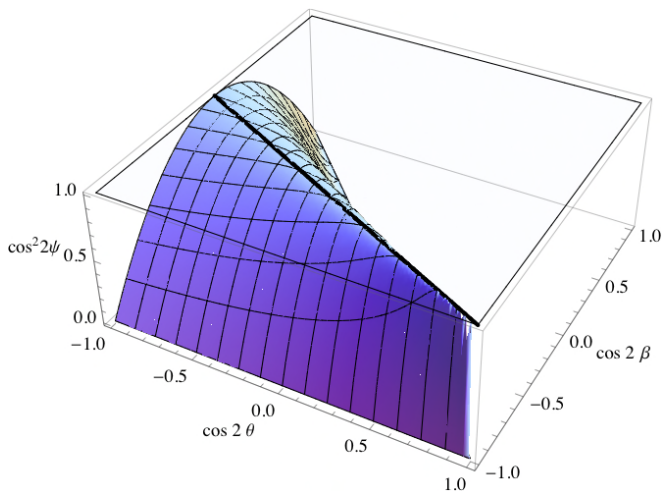


FIG. 7: **Region divisions in coordinate form:** The three ways the binary’s orbital angular momentum can wind around the two null lines are separated by cases where the cone is tangent to one or the other axis. In this figure we express this dividing surface using explicit coordinates for the 3d configuration space: $z = \cos^2 2\psi_J$, $x = \cos 2\theta_J$, $y = \cos 2\beta$. Points on this surface are simultaneous solutions to Eq. (12), as calculated by Eq. (15). In this figure, the R1 region is the largest, farthest from the viewer; the region R3 is the region above the surface, closest to the viewer; and the region R2 is below the surface.

available in the literature; see, e.g., Eqs. (31-37) and Fig. 1 from Buonanno et al. [20]. Additionally, though these expressions can be evaluated in any coordinate system (see, e.g., Fig. 1 in Buonanno et al. [20]), we adopt a specific coordinate system aligned with the total angular momentum. (These coordinates are different from the frame adopted in Eq. (10).) In our coordinate system, the expressions provided in Bu-

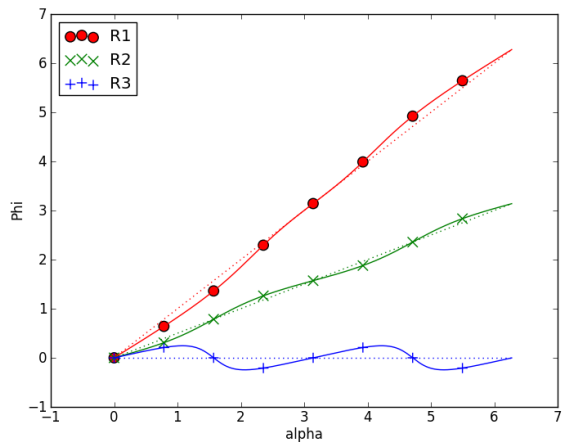


FIG. 8: **Phase evolution versus time:** For three selected viewing geometries of a single binary with $\beta = 60^\circ$, a plot of $\Phi - \Phi_S(t) = \arg(z)$ versus α , the precession phase. This plot shows how much of the precession phase is accumulated in the gravitational-wave signal due to precession [Eq. (21)]. These three phase evolutions are generated from Eqs. (17). The dotted line corresponds to $W\alpha$, where W corresponds to the rate of secular phase increase appropriate to that line of sight. The three viewing geometries lie in the three regions R1,R2,R3 described in the text.

nanno et al. [20] correspond to the expressions below, with their ι corresponding to our β and their Θ corresponding to our θ_J . In these expressions, the angle α is the accumulated precession phase $\int \Omega_p dt$ of the orbital angular momentum around \hat{J} . The reference phase Φ_S used in BCV is given by $\phi_{orb} - \alpha \cos \beta$ for ϕ_{orb} the orbital phase:

$$h \propto (C_+F_+ + C_\times F_\times) \cos(2\phi_{orb} - 2\alpha \cos \beta) + (S_+F_+ + S_\times F_\times) \sin(2\phi_{orb} - 2\alpha \cos \beta) \quad (17a)$$

$$\propto \text{Re}[(C_+F_+ + C_\times F_\times) - i(S_+F_+ + S_\times F_\times)] \times e^{2i(\phi_{orb} - \alpha \cos \beta)} \quad (17b)$$

$$C_+ \equiv \frac{1}{2} \cos^2 \theta_J [\sin^2 \alpha - \cos^2 \beta \cos^2 \alpha] + \frac{1}{2} (\cos^2 \beta \sin^2 \alpha - \cos^2 \alpha) - \frac{1}{2} \sin^2 \theta_J \sin^2 \beta - \frac{1}{4} \sin 2\theta_J \sin 2\beta \cos \alpha \quad (17c)$$

$$S_+ \equiv \frac{1}{2} (1 + \cos^2 \theta_J) \cos \beta \sin 2\alpha + \frac{1}{2} \sin 2\theta_J \sin \beta \sin \alpha \quad (17d)$$

$$C_\times \equiv -\frac{1}{2} \cos \theta (1 + \cos^2 \beta) \sin 2\alpha - \frac{1}{2} \sin \theta_J \sin 2\beta \sin \alpha \quad (17e)$$

$$S_\times \equiv -\cos \theta_J \cos \beta \cos 2\alpha - \sin \theta_J \sin \beta \cos \alpha \quad (17f)$$

with a corresponding expression for the orthogonal polarization. For the calculations needed here, however, the waveform is most usefully expressed as amplitude and phase modulation of a sinusoid:

$$h \propto \text{Re}[Ae^{2i\Phi_{wave}}] = \text{Re}[ze^{2i(\phi_{orb} - \alpha \cos \beta)}] \quad (18)$$

$$\Phi_{wave} = \phi_{orb} - \alpha \cos \beta + \frac{1}{2} \arg z \quad (19)$$

$$z \equiv (C_+F_+ + C_\times F_\times) - i(S_+F_+ + S_\times F_\times) \quad (20)$$

Practically speaking, the phase increases and oscillates with time. The gravitational-wave phase Φ_{wave} can be decomposed into three parts:

$$\Phi_{wave} \equiv \phi_{orb} + W\alpha + \delta\phi_{prec} \quad (21)$$

These three parts are (a) orbital modulation ϕ_{orb} ; (b) a precession-induced secular increase in phase imposed by geometric effects associated with precession ($W\alpha$); and (c) residual modulations in phase caused by precession ($\delta\phi_{prec}$). Both the secular evolution factor W and modulations depend on the line of sight; see Figure 8 for three examples.

The secular phase evolution W is particularly simple. For example, for binaries and viewing orientations where the orbital plane never crosses the line of sight, corresponding to a single helicity being present along the line of sight, the secular phase must accumulate steadily in proportion to this helicity. Using the special case $\theta = 0, \pi$ to determine suitable coefficients, one can show that

$$W = (\text{sign}(\cos \beta) - \cos \beta) \quad (22)$$

More generally, the secular phase factor $2W$ is $-2\cos \beta$ plus an *integer*, related to the number of times the complex number z winds around the point $z = 0$ in a precession cycle (i.e., versus α):

$$W = \frac{1}{2} n_{wind} - \cos \beta = -\cos \beta + \frac{1}{4\pi i} \int \frac{dz}{z} \quad (23)$$

where this integral follows a contour in z corresponding to α evolving from 0 to 2π (i.e., one precession cycle).

Figure 9 shows examples of different trajectories for the complex amplitude $z(t)$. Depending on how the angular momentum winds around the two “null lines” [Figure 6], the

complex number z derived from the angular momentum and the detector orientation can wind around the origin (the point corresponding to \hat{L} along those null lines). This integral can be explicitly evaluated, for example, by substituting $u = e^{i\alpha}$ and performing a contour integral. Since by construction the complex number z is exactly zero at some point on its cycle if and only if Eq. (12) holds, the connected subsets of R1, R2, and R3 are also regions of constant winding number n_{wind} . Keeping in mind the regions have different connected subsets depending on the sign of $\cos \beta$, we evaluate W and find

$$W \equiv -\cos \beta + \begin{cases} \text{sign}(\cos \beta) & \text{R1} \\ \frac{1}{2} \text{sign}(\cos \beta) & \text{R2} \\ 0 & \text{R3} \end{cases} \quad (24)$$

ACST find an approximately comparable result [their Eq. (65); see also and [37]] by integrating an ODE for the phase perturbation due to precession. That expression does not include the region R2 or correctly identify the conditions that cause transition from one secular phase to another.

The complex amplitude $z(t)$ also encodes the way that the gravitational-wave phase and amplitude “oscillate” about their representative values. Binaries whose angular momenta are aligned with their orbit do not precess, so they do not accumulate secular precession phase ($W = 0$, as $z \propto e^{i2\alpha}$) and their phase does not oscillate. As is apparent from the $z(t)$ trajectories in Figure 9, any oscillations in amplitude and phase are more extreme for trajectories passing closer to $z \simeq 0$. These extreme oscillations cannot be well-fit by a non-precessing template. We will show below that the best fitting factor between a precessing signal and a non-precessing template family correlates directly with the amount of phase and amplitude oscillation a signal exhibits.

By way of example, Figure 8 shows how precession introduces additional secular and oscillating contributions to the gravitational wave phase of the *same* binary, seen along different lines of sight. The three curves in this figure show $\arg(z)$ versus α , as extracted from $z(\alpha)$ [Figure 9]. We can clearly see the distinct secular phase trajectories, corresponding to each of the three ways \vec{L} can wind around the “null lines” (equivalently, how $z(t)$ can wind around the origin).

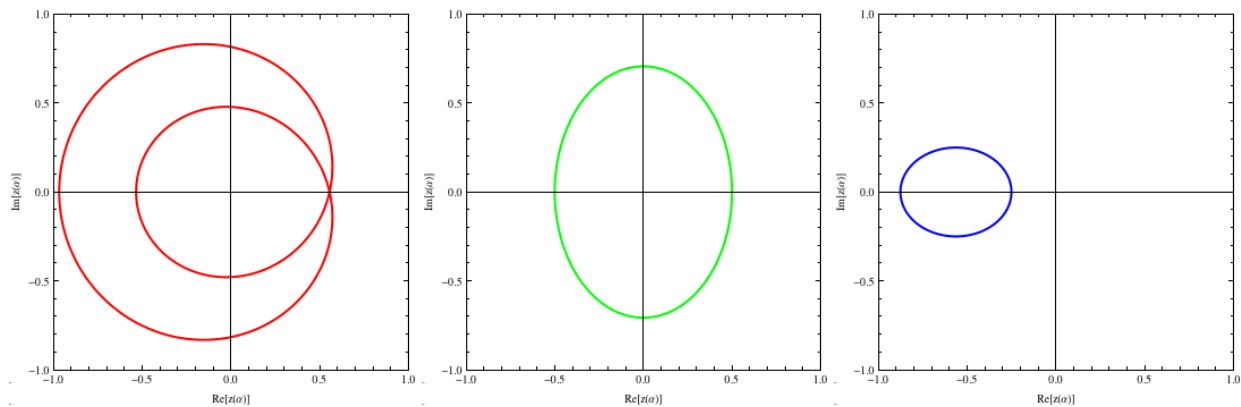


FIG. 9: **Complex amplitude contours:** Three examples of the complex amplitude $z(\alpha)$ over a precession cycle, in the constant precession cone approximation. The three configurations shown correspond to the three fiducial precession cones shown in Figure 6.

V. AVERAGING AMPLITUDE AND MISMATCH WITH THE PRECESSION CONE

In this section we estimate the response of gravitational-wave detectors and non-precessing data analysis strategies to a precessing signal. Using a separation-of-timescales argument, we show that precession-induced modulations *decouple* from the orbital phase, allowing key expressions like the signal amplitude and mismatch against proposed signal templates to be computed by an average over the precession cone. We apply this idea to compute how precession modifies two quantities: the signal strength (SNR) and the mismatch of a non-precessing template with a precessing signal. Combined, these expressions tell us the relative signal strength a data analysis pipeline would recover from a precessing binary, given we know how well it performs for a non-precessing counterpart (i.e., one with similar masses but aligned spins).

The signal-to-noise ratio for the detection of an exact template waveform h_e using an optimal filter constructed from a model waveform h_m used as a template is given by

$$\rho_m = \langle h_e | \hat{h}_m \rangle = \frac{\langle h_e | h_m \rangle}{\langle h_m | h_m \rangle^{1/2}}, \quad (25)$$

where the noise-weighted inner product $\langle h_e | h_m \rangle$ is given by

$$\langle h_e | h_m \rangle = 2 \int_{-\infty}^{\infty} df \frac{\tilde{h}_e(f) \tilde{h}_m^*(f)}{S_n(|f|)}. \quad (26)$$

Here $S_n(|f|)$ is the one-sided power spectral density of the detector strain noise $n(t)$, defined by

$$\langle \tilde{n}(f) \tilde{n}^*(f') \rangle = \frac{1}{2} \delta(f - f') S_n(|f|), \quad (27)$$

and $\tilde{h}(f)$ is the frequency-domain representation of the waveform, given by

$$\tilde{h}(f) = \int_{-\infty}^{\infty} h(t) e^{-2\pi i f t} dt. \quad (28)$$

If we know the exact waveform, the strength of the signal is given by $\rho^2 = \langle h_e | h_e \rangle$. However, if there is an error in the

waveform model h_m , then the signal-to-noise ratio is reduced by a factor

$$\rho_m = M \rho \quad (29)$$

where $0 \leq M \leq 1$ is the match of the model signal. The model waveform $h_m = h_m(\vec{\lambda})$ is a function of the model's intrinsic parameters $\vec{\lambda}$ (e.g. masses, spins, etc.) and extrinsic parameters $\vec{\lambda}_e$ (e.g., time of arrival, coalescence phase, sky location, etc.). The model waveform having the same physical parameters as the exact waveform h_m might not have the highest match, and so we define the fitting factor F as

$$F = \max_{\vec{\lambda}, \vec{\lambda}_e} \langle \hat{h}_e | \hat{h}_m(\vec{\lambda}, \vec{\lambda}_e) \rangle. \quad (30)$$

For the best-fit parameters, the signal-to-noise ratio will be reduced by a factor of $\rho_m = F \rho$.

In this section we use the constant precession cone approximation to derive closed-form expressions for the fitting factor F and the geometrical factors in the signal amplitude ρ^2 . Formally, our approximation arises through separation of timescales. At each instant, the gravitational-wave emission is instantaneously quadrupolar. Expanding in powers of $\Omega_p/\pi f$, the time-domain amplitude modulation $A(t)$ implied by the beam pattern translates directly to frequency-domain modulation $A(t(f))$ [ACST Eq. (36-37)]; see, e.g., Figure 2. Each frequency identifies an orientation of the angular momentum vector $\hat{L}(f)$ and thus precession phase α . So long as a few precession cycles dominate peak emission, a single (effectively “constant”) precession cone dominates as well. Adopting this precession cone as fiducial, we can transform the inner products involving $A(t(f)) = A_o(f) B(\hat{L}(t))$ into inner products involving the “slow” degrees of freedom (i.e., just $A(f)$) and *averages* over the “fast” (precession) degrees of freedom ($B(\hat{L})$). The averages over slow degrees of freedom do not explicitly depend on precession geometry, detector noise, or component masses. The expression factors. We therefore arrive at expressions for ρ^2 and F in terms of averages. As these averages encode all orientation-dependent effects, we emphasize the averages below, keeping in mind that their prefactors

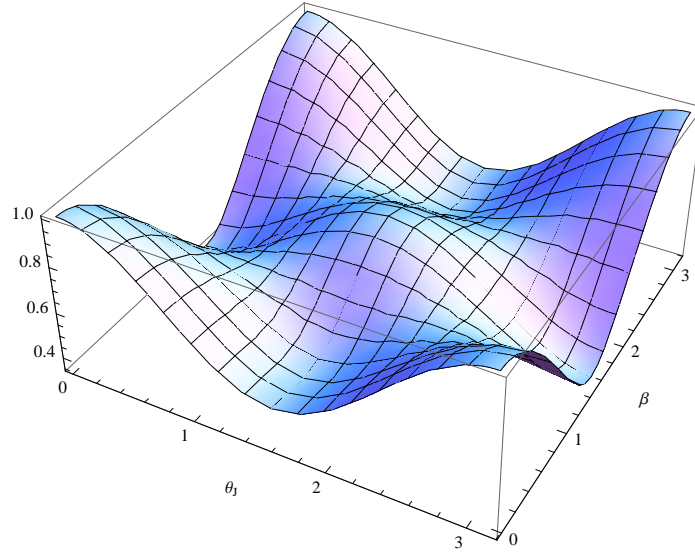


FIG. 10: **Amplitude ratio model:** For spinning precessing binaries, the function $s(\theta_J, \beta, \psi_J = 0)$ describing the average amplitude along a given line of sight, assuming a *steadily precessing* binary with precession cone opening angle β . The function $s(\theta_J, \beta, \psi_J)$ [Eq. (31)] is approximately the ratio ρ/ρ_{ns} between the amplitude ρ of a spinning, precessing binary seen in-band in a configuration and line of sight specified by $(\theta_J, \beta, \psi_J)$ and the amplitude ρ_{ns} of a *nonspinning* binary of comparable masses.

(if needed) can be easily computed once and for all, using a face-on binary.

A. Averaged amplitude

The precession of the beam across the line of sight modulates the amplitude seen at a single detector, in both sin and cos quadratures. We estimate the signal power by adding each quadrature's contribution independently, including the prefactor implied by the orientation of L relative to the line of sight and detector. We then average the resulting expression over the entire precession cone. Compared to the geometrical factor for an optimally oriented non-precessing source, the amplitude ρ^2 is smaller by a factor s^2 :

$$\begin{aligned} s^2(\theta_J, \beta, \psi_J) &= \left\langle \frac{(1 + (\hat{L} \cdot n)^2)^2}{4} \cos^2 2\psi_L(t) + (\hat{L} \cdot n)^2 \sin^2 2\psi_L(t) \right\rangle = \left\langle \frac{(1 + (\hat{L} \cdot n)^2)^2}{4} - \frac{(1 - (\hat{L} \cdot n)^2)^2}{4} \sin^2 2\psi_L(t) \right\rangle \\ &= \left\langle \frac{(1 + (\hat{L} \cdot n)^2)^2}{4} \right\rangle - \langle (\hat{L} \cdot \hat{x})^2 (\hat{L} \cdot \hat{y})^2 \rangle \end{aligned} \quad (31)$$

$$= \frac{1}{1024} [\{c_p(x-1)^2 + x^2\}(35y^2 + 10y - 13) + 2x(5y^2 + 166y + 53) - 13y^2 + 106y + 451] \quad (32)$$

where $x = \cos 2\theta_J$, $y = \cos 2\beta$ and $c_p = \cos 4\psi_J$. Note that all polarization dependence enters through a term $\propto c_p(1-x)^2 + x^2$; the average amplitude is almost polarization-independent near $\theta_J \simeq 0$.

Figure 10 shows how the relative amplitude of a BH-NS binary seen directly overhead a single detector should change, versus the purely geometrical orientation parameters θ, β, ψ_J describing the constant precession cone.

B. Averaging and fitting factor

The phase evolution is more subtle. As simple precession parallel-transport the orbit along a precessing path, the gravitational-wave phase ϕ_{wave} of the *single polarization to which our detector is sensitive* oscillates about a combination of the orbital phase and a secularly accumulating proportion

of the precession phase α :

$$2\phi_{wave} = 2\phi_{orb} + 2\delta\phi_{prec}(\alpha) + 2W\alpha \quad (33)$$

as described above. Finally, the spin also influences the accumulation of orbital phase ϕ_{orb} : the projection of \vec{S}_1 along \vec{L} produces a “gravitomagnetic repulsion”, changing the orbital evolution ϕ_{orb} by slowing the rate of increase in frequency; see, e.g., Eq. (6) in [19].

For detectors like LIGO, which are sensitive to an epoch where the binary's opening angle is nearly constant, the *secular* phase changes (ϕ_{orb} and $W\alpha$) can be well-fit by a *sufficiently generic* non-precessing waveform.⁷ For example, the secular phase evolution of many precessing waveforms can be well-fit by a non-precessing waveform with different chirp mass and mass ratio (\mathcal{M}_c, η). On the other hand, amplitude and phase oscillations in $A(t)$ and $\delta\phi_{prec}$ cannot be fit with non-precessing templates.

Using the ansatz that the best non-precessing template h_m will perfectly reproduce the *secular* phase, the time-averaged overlap between the spinning waveform h_e and the best non-spinning template must be proportional to the best non-spinning fitting factor. We therefore define approximation to the fitting factor F that captures the effects of precession by

$$s\mathcal{F} \equiv \int \frac{dt}{T} \langle h_e(t) | h_m(t) \rangle \quad (34)$$

where s is the average amplitude from Eq. (31) and where the average is over a single precession cycle of \hat{L} in h_e , and where h_m is the best-fitting nonspinning template to the entire cycle. Replacing a time average by an average over the precession phase α and the true signal $h_e(t)$ with the nonspinning template times the amplitude and (fourier domain) precession phase terms A and $\delta\phi$ described above, this expression reduces to an average of the oscillating amplitude and phase over the cycle:

$$s\mathcal{F} = \max_{\phi_o} \int A \cos(2\delta\phi + \phi_o) d\alpha / (2\pi) \quad (35)$$

We will provide a closed-form expression in the next section. However, to understand that result, it is helpful to think directly in terms of this integral. For example, in the limit of small amplitude and phase modulations occurring periodically on the precession cone, a non-precessing template model should fit them to no better than

$$\mathcal{F} \simeq 1 - \frac{1}{2} \left[\langle (\delta\phi)^2 \rangle + \langle (\delta A/A)^2 \rangle - \langle \delta A/A \rangle^2 \right] \quad (36)$$

[This expression can be rederived directly from the original integral.] In particular, the amplitude and phase modulations introduced by precession inevitably diminish the ability of a non-precessing template to match them, by an amount proportional to the standard deviation of oscillations in time and phase about the reference model.

Oscillations in phase and amplitude are most extreme for binary geometries near the boundaries between regions. A non-precessing signal should be maximally unable to match the large phase and amplitude variations near this surface. For example, a signal on the surface has different epochs, separated by zeros of the (complex) amplitude. A non-precessing

signal can coherently reproduce the phase trend in one portion of the signal or the other, but not both.

C. Constant Precession Cone

In the limit of a constant precession cone, the integral can be performed analytically. Replacing a time average by an average over the precession phase α and the true signal $h(\hat{L})$ with the nonspinning template times the amplitude and (fourier domain) precession phase terms A and $\delta\phi$ described above, the angle-averaged expression reduces

$$s\mathcal{F} = \sqrt{(s\mathcal{F}_s)^2 + (s\mathcal{F}_c)^2} \quad (37)$$

where in the second line we convert maximization of the integrand over ϕ_o into two integrals.

$$s\mathcal{F}_c \equiv \int A_{tot} \cos 2\delta\phi \frac{d\alpha}{2\pi} \quad (38)$$

$$s\mathcal{F}_s \equiv \int A_{tot} \sin 2\delta\phi \frac{d\alpha}{2\pi} \quad (39)$$

This expression reduces to a simple contour integral:

$$s\mathcal{F}_c \equiv \int \frac{(z/Z + (z/Z)^*)}{2} \frac{d\alpha}{2\pi} \quad (40)$$

$$s\mathcal{F}_s \equiv \int \frac{((z/Z) - (z/Z)^*)}{2i} \frac{d\alpha}{2\pi} \quad (41)$$

$$z(\alpha) \equiv A_{tot} e^{i2(\delta\Psi + \alpha W)} \quad (42)$$

$$Z(\alpha) \equiv e^{i2W\alpha} \quad (43)$$

where z is the complex representation of the waveform amplitude and phase given in Eq. (20), while dividing by Z is equivalent to subtracting the secular phase. Using the complex variable $u = e^{i\alpha}$ to represent $Z = u^{2W} = u^{n_{wind}}$ and the sinusoids in $C_{+,x}$ and $S_{+,x}$ analytically via $\cos \alpha = (u + 1/u)/2$ and similarly, we find the fitting factor predicted can be calculated using the contour integral

$$s\mathcal{F} = |I| \quad (44)$$

$$I \equiv \int \frac{z/Z d\alpha}{2\pi} = \int \frac{z/u^{n_{wind}} du}{2\pi i u} \quad (45)$$

This trivial contour integral corresponds to identifying terms $\propto u^n$ in z for different n . The value of this contour integral depends discontinuously on the winding number n_{wind} . Using the definitions of C, S to perform this integral, we find

$$I \equiv \begin{cases} -\frac{3}{4} \cos 2\psi_J \sin^2 \beta \sin^2 \theta & n_{wind} = 0 \\ \mp \frac{(2 \sin \beta \pm \sin 2\beta)(\cos 2\psi_J \sin 2\theta \mp 2i \sin \theta \sin 2\psi_J)}{8} & n_{wind} = \pm 1 \\ -\frac{(1 \pm \cos \beta)^2}{8} [\cos 2\psi_J (1 + \cos^2 \theta) \mp 2i \cos \theta \sin 2\psi_J] & n_{wind} = \pm 2 \end{cases} \quad (46a)$$

Finally, we estimate the fitting factor for all angles by dividing this closed-form expression by the closed-form expression for s :

$$\mathcal{F}(\theta_J, \beta, \psi_J) \equiv |I(\theta_J, \beta, \psi_J)|/s(\theta_J, \beta, \psi_J) \quad (46b)$$

This ratio varies strongly in all three parameters and is best summarized by the explicit expression above. Though complicated, some important physical lessons can be drawn. First and foremost, for non-precessing signals the predicted fitting factor is $F = 1$. Second and most critically, while the predicted fitting factor has a local extremum with $\mathcal{F} \simeq 1$ in each of the three regions, the predicted fitting factor drops rapidly as we approach the surface dividing them: at the surface defined by Eq. (15) and shown in Figure 7. In other words, this expression suggests the worst possible matches will occur when the angular momentum at some point in the precession cycle is along one of the two null lines. As noted above, the low fitting factor in this region occurs because the signal consists of comparable amounts of power with two competing and incompatible secular phase trends. Finally, under special conditions such as $\theta \simeq 0$ in R2 and R3, this expression predicts pathologically low matches $P \simeq 0$. As we will discuss at greater length in a forthcoming publication, an empirically more successful approximation replaces the options in I by the the maximum over the three options.

Though derived under the seemingly-strong expression of a constant precession cone, we have verified this expression applies to a broad family of real BH-NS inspirals, by calculating the overlap between the gravitational radiation emitted from non-precessing and precessing binaries and maximizing over the non-precessing signal's parameters. We will describe these Monte Carlo studies in more detail in a subsequent publication. In brief, these studies corroborate many earlier studies that examined how well non-precessing signals recover precessing waveforms [20, 31, 37]. First, in special but not uncommon circumstances, fitting factors as low as 0.6 occur. Second, small fitting factors (i.e., large mismatches) can occur even with small amounts of spin-orbit misalignment, though they become more common as misalignment increases. For nearly aligned binaries, signals with the lowest match correspond to directions with low signal power. Contrary to previous claims, however, we identify some configurations with both low fitting factor and significant signal power along the line of sight.

This analytic study differs from all previous investigations in that we assume a non-precessing signal model can always match any secular phase evolution; identify which precessing configurations lead to large modulations; and quantify the expected purely geometrical effect these modulations have on the fitting factor. As an example, in Figure 11 we predict the distribution of fitting factors expected when a non-precessing

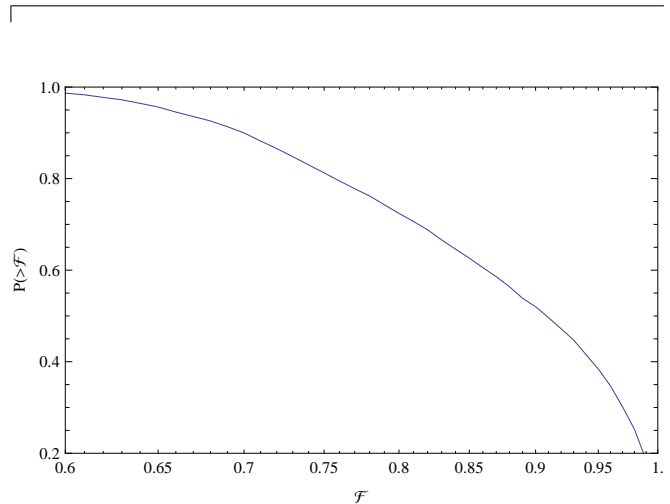


FIG. 11: **Distribution of fitting factors for single-spin BH-NS:** Using only the analytic expressions provided in this paper, the predicted fraction $P(> \mathcal{F})$ of fitting factors greater than \mathcal{F} for a randomly oriented BH-NS binary with $m_1 = 10M_\odot, m_2 = 1.4M_\odot$, with the dimensionless black hole spin χ_1 randomly oriented and with magnitude uniformly distributed between 0 and 0.98. Compare to the solid line in the bottom right panel of Figure 9 in [31], although there the neutron star also has a spin up to 0.3.

search is applied to randomly-oriented BH-NS binary. Despite the simplicity of our model, we recover quantitatively similar results to previous studies [31]. Unlike earlier studies, however, our expressions allow us both to identify precisely which binaries are least well fit and to understand precisely why.

D. Validating our approximations with Monte Carlo

To demonstrate that our approximation works, we have compared randomly-chosen BH-NS binaries with a standard non-precessing template bank: Taylor F2 templates with physical parameters, hexagonal template bank chosen for 97% minimal match; and a likely early advanced LIGO noise curve, the low-power zero-detune PSD [41] such that $f_{peak} \simeq 40$ Hz.

For example, Figure 12 shows the results for 30000 BH-NS binaries ($10M_\odot + 1.4M_\odot$) with random orientations for $\kappa = \hat{L} \cdot \hat{S} > -1/2$ and spin magnitudes $a_1 \in [0, 1]$. The limit on κ removes some systems with transitional preces-

sion for clarity; in the next figure, we allow nearly the full range of κ . The bottom panel shows the configurations of the worst-fit sources for two polarizations (J nearly aligned with the detector on the plane of the sky and 45° off the detector arms). Both cluster near the predictions of our model (dotted lines): our approximation correctly identifies the worst-fit locations. More generally, the top panel shows our estimate works (nearly) everywhere: it compares our fitting factor estimate \mathcal{F} to the fitting factor F calculated by comparing that signal the template bank. Despite known systematic differences between the signal and template model even for aligned systems, our match prediction works well almost everywhere. For comparison, the vertical dotted line at -0.03 shows the typical mismatch expected from template bank discreteness.

In this comparison, we have artificially eliminated the small fraction of worst-performing configurations, corresponding to sources recovered with templates near the edge of the template bank where $\eta = 1/4$. The secular phasing due to the aligned component of the spin is best fit by templates with η biased to larger than its true value. Due to the finite parameter extent in η of physical Taylor F2 templates, the conventional signal model fails to capture even the secular effects of large aligned spins. An aligned but non-precessing template bank would however be able to capture these signals. To faithfully reproduce signals with aligned spins using standard template banks, we must extend the bank into $\eta > 1/4$. This nearly captures the secular effect of aligned spins, and is a reasonably good substitute for a true aligned spin template bank. Figure 13 shows the results of this extended- η bank, compared to a much larger set of BH-NS binaries. The top panel shows that our approximation continues to work well for generic sources, even given systematic differences between signal and template and the absence of spin. In particular, the bottom panel demonstrates that except for rare outliers, our approximation correctly identifies the worst-fit sources.

E. Beyond the constant precession cone

Though we emphasize the value of a (nearly-)constant precession cone in approximating binary inspiral, the concepts and expressions we provide apply equally well to many simply-precessing binaries. As an example, in Figure 14 we show the precession-induced phase evolution for two systems with slightly different β , such that they are near a transition between regions. One is in R1 and the other in R2. The nearness to the transition surface causes large oscillations around the secular increase in phase. Binaries whose opening angles $\beta(f)$ evolve across these boundaries and particularly across $\pi/2$ in band can undergo dramatic transitions in the properties of their observable waveform, accumulating only one helicity early on and another helicity later.

VI. CONCLUSIONS

In this paper we have explored two features of the gravitational-wave signal seen by ground-based detectors in

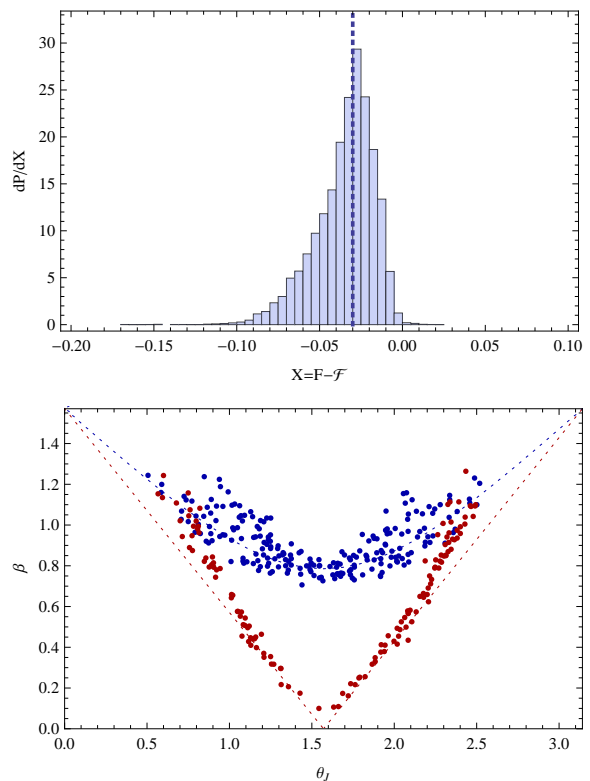


FIG. 12: Comparison of the analytic prediction of Sec. V.C with numerical results I: Single binary masses and spin magnitude *Top panel:* For 30000 BH-NS binaries ($10M_\odot + 1.4M_\odot$ with $a_1 \in [0, 1]$) with random orientations for $\hat{L} \cdot \hat{S} > -1/2$, a comparison between our estimate \mathcal{F} and the fitting factor F calculated by comparing that signal with a standard single-detector template family (Taylor F2 templates with physical parameters; hexagonal template bank chosen for 97% minimal match; early-stage advanced LIGO noise curve such that $f_{peak} \simeq 40$ Hz [41]). For comparison, the vertical dotted line at -0.03 shows the typical mismatch expected from template bank discreteness. Despite known systematic differences between the signal and template model even for aligned systems, our match prediction works well almost everywhere. To highlight its effectiveness, we have eliminated the small fraction of worst-performing configurations, corresponding to sources recovered with templates with $0.24 < \eta \leq 1/4$. Due to the finite parameter extent of physical Taylor F2 templates, the conventional signal model cannot reproduce large aligned spins. *Bottom panel:* For the same comparison of template bank against signals as above, the configurations of the worst-fit sources ($F < 0.7$) with $\cos 4\psi > 0.9$ (blue; J nearly aligned with the detector on the plane of the sky) and $\cos 4\psi < -0.9$ (red; J nearly 45° off the detector arms, in the plane of the sky). For comparison, the blue and red solid lines are the surfaces $\cos 2\beta + \cos^2 \theta = 0$ (blue) and $\cos 2\theta_J + 2 \cos 2\beta$ (red) [Eq. (16)]. These lines are two one-dimensional cuts through the surface separating R1 and R2, where our expression predicts the worst single-detector matches will occur.

a “constant precession cone” limit. We compare their amplitude to similar face-on non-precessing binary; we compare their waveform to the best-fitting non-precessing signal. We find closed-form expressions for both quantities. Our expressions involve only geometrical parameters – the orientation of

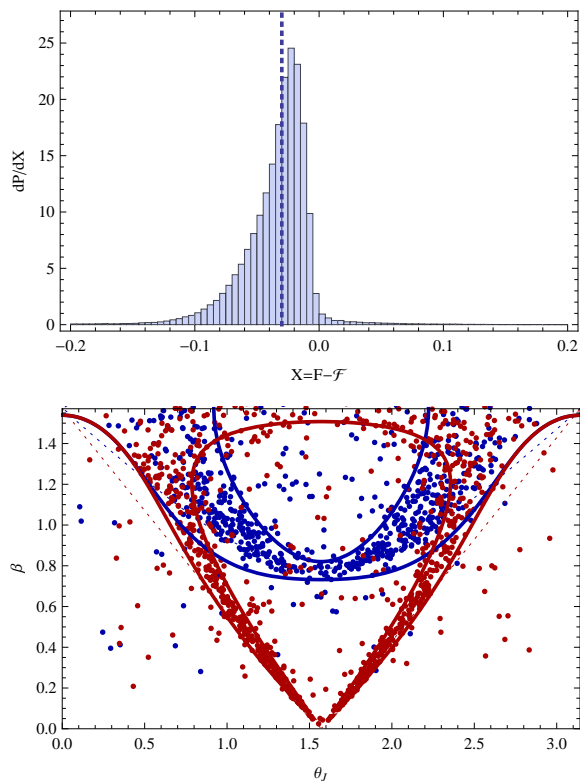


FIG. 13: **Comparison of the analytic prediction of Sec. V.C with numerical results II:** Monte Carlo. As Figure 12, except (a) the injected signal can have generic BH-NS-like masses $m_1 \in [3, 15]M_\odot$, $m_2 \in [1, 5]M_\odot$, dimensionless spin magnitudes $\chi \in [0, 1]$, and spin-orbit misalignments $\hat{L} \cdot \hat{S} > -0.9$; (b) to better recover aligned-spin signals, the template family includes Taylor F2 waveforms with $\eta > 1/4$, spaced in chirp mass and η according to the 2PN hexagonal template bank. *Top panel:* Our match prediction works for generic sources. [Because the mass and spin distribution used in this analysis favors low γ and thus binaries nearly aligned in band, this distribution partially reflects our ability to recover nearly-aligned-spin binaries with an extended η Taylor F2 bank. That said, subsets of the sample bounded below in γ also demonstrate our prediction works well for generic binaries with significant in-band misalignment.] *Bottom panel:* Our expression identifies the dominant physical mechanisms that produce a poor fit between a spinning binary and a candidate non-precessing waveform. Like Figure 12, the dotted lines show the separatrices between regions. The *solid lines* show the contours predicted from our expression for $\mathcal{F} = 0.75$ and $\psi = 0$ (blue) or $\psi = \pi/4$ (red). For comparison, the points indicate all signal versus bank fitting factors $F < 0.66$ for $\cos 4\psi > 0.975$ (blue) or $F < 0.7$ for $\cos 4\psi < -0.975$.

the precession cone relative to the line of sight – with no explicit reference to the (post-Newtonian) phase model, detector noise curve, or binary parameters. In a subsequent paper we will use these factors to interpret the selection biases of optimal and non-precessing searches for precessing binaries. This publication will provide explicit Monte Carlo over all possible source parameters and sky locations and calculate overlaps using state-of-the-art signal models.

In this paper we provide only the leading-order geometric

influence that the precession cone has on signal amplitude.

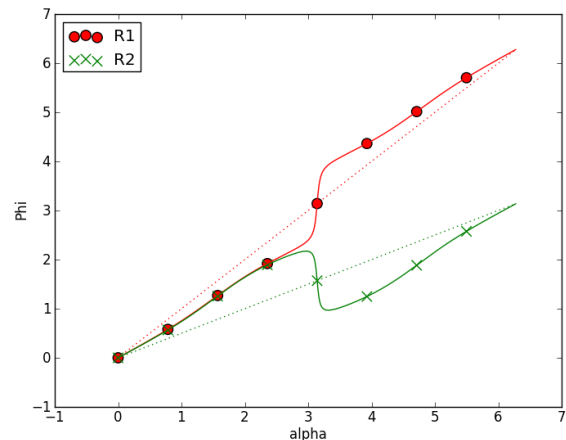


FIG. 14: **Discrete phase change:** With a fixed viewing geometry, the geometrical phase difference $\arg(z)$ on either side of a transition surface (here, R1 to R2). As in Figure 8, an entire precession cycle is shown.

Additionally, the same spin misalignments that allow the binary’s orbit to precess also diminish the binary’s inspiral time, compared to an aligned non-precessing signal. We will describe a more complete model for the spin-dependent signal amplitude ρ^2 in a future paper.

Finally, in this paper we point out that non-precessing signals often fit precessing signals’ *secular* phase evolution. The secular evolution of (single-detector) gravitational-wave phase depends on the line of sight to the source and orientation of the detector (W). As a result, two independent detectors running two independent searches may identify two very different best-fitting (non-precessing) signals, due only to the detectors’ orientations. These biases in recovered parameters must be taken into careful account when constructing coincidence-based search algorithms. We will also address biases in recovered parameters in a future paper.

Acknowledgments

The authors benefitted from helpful feedback from Tom Dent, Jacob Slutsky, and Evan Ochsner. DB and AL are grateful to NSF award PHY-0847611 for support. Additionally, AL is grateful to NSF grant PHY-0855589. DB is supported by a Cottrell Scholar award from the Research Corporation for Science Advancement. ROS is supported by NSF award PHY-0970074, the Bradley Program Fellowship, and the UWM Research Growth Initiative. ROS was also supported by NSF award PHY-0653462 and the Penn State Center for Gravitational Wave Physics. Computations used in this work were performed on the Syracuse University Gravitation and Relativity cluster, which is supported by NSF awards PHY-1040231, PHY-0600953 and PHY-1104371.

-
- [1] B. Abbott et al. (LIGO Scientific), Rept. Prog. Phys. **72**, 076901 (2009).
- [2] D. Shoemaker (the Advanced LIGO Team), *Advanced LIGO Reference Design* (2009), [LIGO-M060056].
- [3] G. M. Harry and the LIGO Scientific Collaboration, Class. Quant. Grav. **27**, 084006 (2010).
- [4] T. Accadia, F. Acernese, F. Antonucci, P. Astone, G. Ballardin, et al., Class. Quant. Grav. **28**, 114002 (2011).
- [5] The Virgo Collaboration, *Advanced Virgo Baseline Design* (2009), [VIR-0027A-09].
- [6] B. Abbott et al. (LIGO Scientific Collaboration), Phys. Rev. **D69**, 122001 (2004).
- [7] B. Abbott et al. (LIGO Scientific Collaboration), Phys. Rev. **D72**, 082001 (2005).
- [8] B. Abbott et al. (LIGO Scientific Collaboration), Phys. Rev. **D73**, 102002 (2006).
- [9] B. Abbott et al. (LIGO Scientific Collaboration), Phys. Rev. **D73**, 062001 (2008).
- [10] B. Abbott et al. (LIGO Scientific Collaboration), Phys. Rev. **D78**, 042002 (2008).
- [11] B. Abbott et al. (LIGO Scientific Collaboration), Phys. Rev. **D77**, 062002 (2008).
- [12] B. P. Abbott et al. (LIGO Scientific Collaboration), Phys. Rev. **D79**, 122001 (2009).
- [13] B. Abbott et al. (LIGO Scientific Collaboration), Phys. Rev. **D80**, 047101 (2009).
- [14] J. Abadie et al. (The LIGO Scientific Collaboration and the Virgo Collaboration), Phys. Rev. **D83**, 122005 (2011).
- [15] J. Abadie et al. (The LIGO Scientific Collaboration and the Virgo Collaboration) (2011).
- [16] J. Abadie et al. (LIGO Scientific Collaboration, Virgo Collaboration), Class. Quant. Grav. **27**, 173001 (2010).
- [17] K. G. Arun, A. Buonanno, G. Faye, and E. Ochsner, Phys. Rev. D **79**, 104023 (2009), 0810.5336.
- [18] A. Buonanno, Y. Chen, Y. Pan, and M. Vallisneri, Phys. Rev. D **70**, 104003 (2004).
- [19] Y. Pan, A. Buonanno, Y. Chen, and M. Vallisneri, Phys. Rev. D **69**, 104017 (2004).
- [20] A. Buonanno, Y. Chen, and M. Vallisneri, Phys. Rev. D **67**, 104025 (2003).
- [21] A. Buonanno, Y. Chen, Y. Pan, H. Tagoshi, and M. Vallisneri, Phys. Rev. D **72**, 084027 (2005).
- [22] M. Hannam, S. Husa, B. Brügmann, and A. Gopakumar, Phys. Rev. D **78**, 104007 (2008).
- [23] A. Buonanno, B. Iyer, E. Ochsner, Y. Pan, and B. Sathyaprakash, Phys. Rev. **D80**, 084043 (2009).
- [24] B. J. Owen, Phys. Rev. D **53**, 6749 (1996).
- [25] B. J. Owen and B. S. Sathyaprakash, Phys. Rev. D **60**, 022002 (1999).
- [26] C. van den Broeck, D. A. Brown, T. Cokelaer, I. Harry, G. Jones, B. S. Sathyaprakash, H. Tagoshi, and H. Takahashi, Phys. Rev. D **80**, 024009 (2009).
- [27] T. Cokelaer, Phys. Rev. D **76**, 102004 (2007).
- [28] B. Allen, W. G. Anderson, P. R. Brady, D. A. Brown, and J. D. E. Creighton (2012), gr-qc/0509116.
- [29] A. Buonanno, Y. Chen, and M. Vallisneri, Phys. Rev. D **67**, 024016 (2003).
- [30] T. Cokelaer, Classical and Quantum Gravity **24**, 6227 (2007).
- [31] P. Ajith, Phys. Rev. D **84**, 084037 (2011), 1107.1267.
- [32] L. E. Kidder, C. M. Will, and A. G. Wiseman, Phys. Rev. D **47**, 4183 (1993).
- [33] E. Poisson and C. M. Will, Phys. Rev. D **52**, 848 (1995).
- [34] L. Blanchet, A. Buonanno, and G. Faye, Phys. Rev. D **74**, 104034 (2006).
- [35] T. A. Apostolatos, C. Cutler, G. J. Sussman, and K. S. Thorne, Phys. Rev. D **49**, 6274 (1994).
- [36] M. Boyle, R. Owen, and H. P. Pfeiffer, Phys. Rev. D **84**, 124011 (2011), 1110.2965.
- [37] T. A. Apostolatos, Phys. Rev. D **52**, 605 (1995).
- [38] L. E. Kidder, Phys. Rev. D **52**, 821 (1995).
- [39] J. D. Schnittman, Phys. Rev. D **70**, 124020 (2004).
- [40] D. Lorimer, Living Reviews in Relativity **2008-8** (2008).
- [41] LIGO Scientific Collaboration (2009), URL <https://dcc.ligo.org/cgi-bin/DocDB/ShowDocument?docid=2974>.
- [42] C. M. Will and A. G. Wiseman, Phys. Rev. D **54**, 4813 (1996), arXiv:gr-qc/9608012.